

Segmentation and Visualization of Flooded Areas Through Sentinel-1 Images and U-Net

Fernando Pech-May^{ID}, Raúl Aquino-Santos^{ID}, Omar Álvarez-Cárdenas^{ID}, Jorge Lozoya Arandia^{ID}, and German Ríos-Toledo^{ID}

Abstract—Floods are the most common phenomenon and cause the most significant economic and social damage to the population. They are becoming more frequent and dangerous. Consequently, it is necessary to create strategies to intervene effectively in the mitigation and resilience of the affected areas. Different methods and techniques have been developed to mitigate the damage caused by this phenomenon. Satellite programs provide a large amount of data on the earth's surface, and geospatial information processing tools help manage different natural disasters. Likewise, deep learning is an approach capable of forecasting time series that can be applied to satellite images for flood prediction and mapping. This article presents an approach for flood segmentation and visualization using the U-Net architecture and Sentinel-1 synthetic aperture radar (SAR) satellite imagery. The U-Net architecture can capture relevant features in SAR images. The approach comprises various phases, from data loading and preprocessing to flood inference and visualization. For the study, the georeferenced dataset Sen1Floods11 is used to train and validate the model through different epochs and training. A study area in southeastern Mexico that presents frequent floods was chosen. The results demonstrate that the segmentation model achieves high accuracy in detecting flooded areas, with promising metrics regarding loss, precision, and F1-score.

Index Terms—Deep learning (DL) and Sentinel-1, flood mapping, flood segmentation, flood with deep learning, Sentinel-1, U-Net and natural disasters.

I. INTRODUCTION

RECENT studies from the Centre for Research on the Epidemiological Disaster indicate that natural disasters have increased [1], [2]. The ravages of this phenomenon cause human losses, considerable economic damage to infrastructure, and different collateral damages to entire population, both rural and urban, which puts approximately 26 million people into

Manuscript received 7 December 2023; revised 29 January 2024 and 26 March 2024; accepted 31 March 2024. Date of publication 11 April 2024; date of current version 1 May 2024. (Corresponding author: Raúl Aquino Santos.)

Fernando Pech-May is with the Computer Systems Department, Instituto Tecnológico Superior de los Ríos, Balancán, Tabasco 86930, Mexico (e-mail: peiwh@semi.ac.cn).

Raúl Aquino-Santos is with the General Coordination of Scientific Research, Universidad de Colima, Colima, CO 28017, Mexico (e-mail: aquinor@ucol.mx).

Omar Álvarez-Cárdenas is with the Telematics Faculty, Universidad de Colima, Colima, CO 28040, Mexico (e-mail: xe1aom@ucol.mx).

Jorge Lozoya Arandia is with the Computacional Science and Technological Inovation Department, Universidad de Guadalajara, Guadalajara, Jalisco 44100, Mexico (e-mail: Jorge.larandia@academicos.udg.mx).

German Ríos-Toledo is with the Sistemas y Computación, Tecnológico Nacional de México campus Tuxtla Gutiérrez, Tuxtla Gutiérrez, Chiapas 29038, México (e-mail: german.rt@tuxtla.tecnm.mx).

Digital Object Identifier 10.1109/JSTARS.2024.3387452

poverty annually [3]. Nevertheless, what is the reason for the increase in these disasters? There are many factors, but without a doubt, climate change and human activities are triggering factors. In 2021, 432 disasters occurred, causing almost 11 000 deaths; 223 were floods (see Fig. 1). In 2022, there were 387 disasters and nearly 31 000 deaths; 176 were floods. Floods have the most significant impact of these catastrophes, affecting more than 45% of the world's population (see Fig. 2) [4].

The countries that suffer the most from floods are India, China, Afghanistan, Germany, and Western Europe [1]. It also significantly impacts food production since it causes losses in crops and livestock, affecting food sovereignty in different countries [5], [6]. Mexico is no stranger to these catastrophes. The climate impact, whether of natural origin or due to human activities, has increased susceptibility in various regions of the country. Hydrometeorological phenomena have increased in the southeastern areas and the coast of the Gulf of Mexico. Therefore, floods have triggered catastrophes, causing severe damage to economic and industrial infrastructure and the well-being of the region's inhabitants [7]. The most severe cases occurred in October 2007 and November 2020. According to official data from the Economic Commission for Latin America and the Caribbean [8], the damage caused in 2007 was US\$3B: 31.77% in the productive sector, 26.9% in agriculture, and 0.5% in the environment. In 2020 [9], more than 800 000 people were affected, 200 400 homes were damaged, and more than US\$1M in emergency response.

The factors that cause flooding can be diverse [10]: 1) pluvial, the result of excess precipitation; 2) fluvial, increase in water levels in rivers, seas, or water bodies; 3) failures of hydraulic works, breaking of dams, dikes, or banks; and 4) failure of natural drainage when the soil can no longer absorb more water.

Given the devastation caused by floods, timely information on the occurrence of floods and their impact on the population is needed. In this sense, flood prediction, identification, and mapping are fundamental. This will allow the authorities to act promptly to implement rescue services, damage assessment, and identification of affected areas for the prompt relief of the population and, in general, the resilience of populations affected by floods.

In recent years, remote sensing has shown notable growth due to its ability to obtain terrestrial data through sensors and cameras implemented on satellites or satellite programs [11], [12], [13], [14]. Satellite programs generally have two types of sensors: passive, which captures optical images, and active,

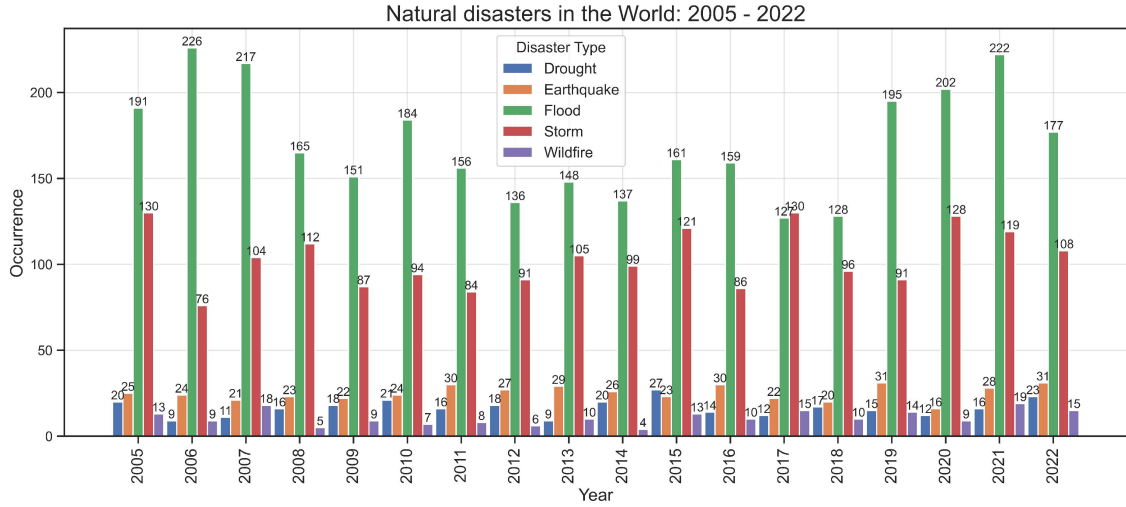


Fig. 1. Occurrence of the five most common natural disasters in the world from 2005 to 2022: Floods, storms, earthquakes, droughts, and wildfires.

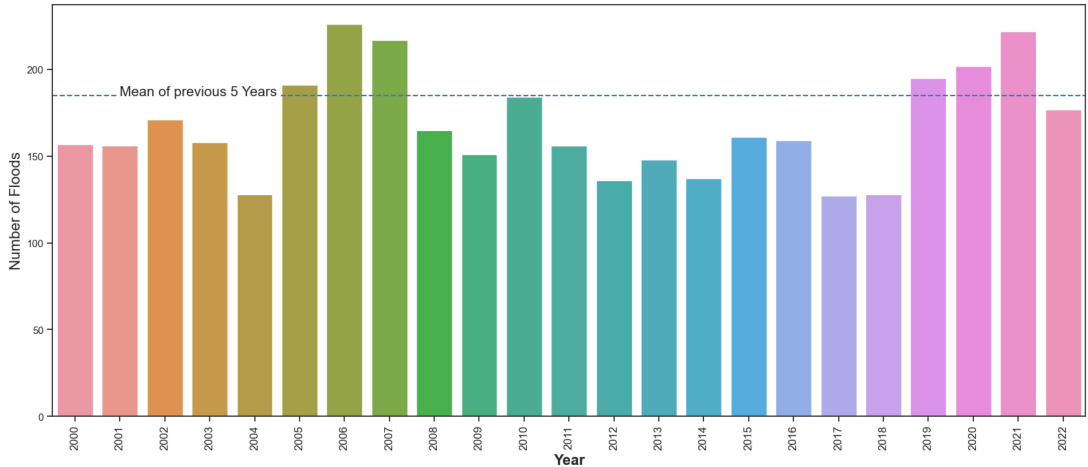


Fig. 2. Floods in the world: 2000–2022. The years 2006, 2007, and 2021 have been the years with the highest flooding in different regions of the world.

which captures radar images. The optical images are high-resolution multispectral and are correlated with the open water surface. However, they can be affected by the presence of clouds during precipitation, making it impossible to acquire clean and reliable images. In contrast, radar images can penetrate clouds and operate day and night and in any weather conditions. This is because the sensors operate at longer wavelengths and are independent of solar radiation. This makes it ideal for monitoring and mapping floods and estimating the damage caused. Satellite programs include Copernicus [14], Landsat [12], and Terra/Aqua (MODIS) [13].

Copernicus stands out for its remarkable capacity to acquire remote data with high temporal and spatial resolution. It is made up of satellites for different purposes: Sentinel-1 provides synthetic aperture radar (SAR) images helpful in observing the earth and oceans; Sentinel-2 provides multispectral optical terrestrial images; Sentinel-3 for marine and land observation; Sentinel-4 and 5 for air quality monitoring; and Sentinel-6 for marine observation [15], [16], [17].

These satellite data have different properties such as: 1) spatial resolution, which determines the area of the earth's surface covered by each pixel of the image; 2) spectral resolution, which represents the electromagnetic spectrum captured by the remote sensor and the number and width of regions; and 3) temporal resolution, which determines how long satellite information can be obtained from the exact location with the same satellite and radiometric resolution [18].

In addition, artificial intelligence algorithms are being used to analyze these data. Both technologies are being used to study climate change, precipitation, carbon flow prediction, drought forecasting, detection of soil changes, earthquakes, bodies of water, floods, crops, etc.

Specifically, deep learning (DL) algorithms have taken on a highly relevant role due to their ability to discriminate data and automate and improve the precision of tasks such as image classification, element detection, and generating thematic cartographic representations [19]. Furthermore, they can learn from feature representations appropriate for classification tasks

of spatial learning using convolutional neural networks (CNNs) and sequential learning using recurrent neural networks (RNNs). These approaches have presented better results compared to other techniques. However, they suffer from some problems. CNNs suffer from inductive biases, while RNNs suffer from gradient disappearance [20]. Furthermore, satisfactory results of DL algorithms require an extensive dataset for training [21], [22]. Due to this need, labeled image datasets have been used.

Some datasets used in different proposals for flood analysis and mapping are Sen1Floods11 [23], which has Sentinel-1 and Sentinel-2 images of 11 manually labeled flood events; UNOSAT [24], with Sentinel-1-SAR labeled images over 15 flood events; OMBRIA [25], with images labeled Sentinel-1 and Sentinel-2 over 23 floods; SEN12-FLOOD [26] with images labeled Sentinel-1 and Sentinel-2; and World Floods that contains information on 119 floods that occurred from 2015 to 2019. These datasets are used in different flood analysis proposals [21], [25], [27], [28], [29].

Free access to these data has allowed various institutions to expand their research using large volumes of data. Satellite data are an effective tool for estimating damage caused by natural disasters and improving risk management. This is due to the sensors' different resolutions and capture methods on space platforms. This data availability has led to developing services that enable the rapid creation of flood maps using automated or semiautomated processes. However, these methods present some uncertainties due to the need for more verification and the rapidity with which they occur.

This article explores a strategy for flood segmentation based on the U-Net architecture and the Sen1Floods11 georeferenced dataset. This is done to segment and visualize flooded areas through satellite images. The study area belongs to southeastern Mexico, which has experienced severe flooding.

II. RELATED WORKS

As a strategy for flood mapping, remote sensing has shown promising results [27], [29], [30], [31]. Many works propose analyses, classifying, detecting, and mapping floods and water bodies using optical (multispectral) or SAR images. Others combine SAR and optical data. Despite promising results, there are still difficulties in satellite images, such as their spatial [32] and temporal resolution [33]. Artificial intelligence also provides different supervised, unsupervised, and contrastive algorithms for flood analysis using satellite images [33], [34]. Deep neural networks, specifically CNNs, are the most widely used [35]. In this sense, the more training data the CNNs have, the better results they will obtain [36].

Regardless of the strategy of the proposed approaches, they have a fundamental premise: the analysis of floods in different locations. Some map floods to coordinate rescue efforts, others analyze flood extents to mitigate and predict their effects, etc.

Generally, traditional machine learning approaches use optical images [5], [37], [38], [39]. Spectral indices are applied to images based on the interactions between vegetation and the electromagnetic energy of the shortwave infrared and

near-infrared spectrum bands [40], [41]. These indices apply to images with different resolutions, such as Landsat, Spot, or Sentinel [42]. However, to map bodies of water and soil vegetation, the following are mainly used: the normalized difference vegetation index [43] and the normalized difference water index [44]. Although optical sensors are highly correlated with open water surfaces, they cannot penetrate clouds, which limits them in rainy or cloudy weather. Consequently, it is impossible to acquire high-resolution, multispectral, cloud-free images. Deroliya et al. [45] present an approach for flood risk mapping considering geomorphic descriptors. They used three algorithms: decision tree, random forest (RF), and gradient-boosted decision trees. Zhou et al. [46] use a support vector machine (SVM); Tulbure et al. [47] and Schumann et al. [48] RF for the analysis of water bodies. Pech-May et al. [5] analyze the behavior of land cover and water bodies of floods in the rainy season using multispectral images and RF, SVM, and classification and regression trees algorithms. Anusha and Bharathi [49] use multispectral imaging with the algorithms mentioned earlier. Konapala et al. [50] presented a strategy for flood identification from SAR satellite images. Rudner et al. [51] used Sentinel-1 and Sentinel-2 to identify flooded areas. Li et al. [52] conducted a study analyzing the damage caused by hurricanes.

Most current approaches use CNNs. They rely on dimensionality reduction to reduce the number of parameters and preserve the relative locations of pixels. Increasing the depth of CNNs can improve their performance because deep networks incorporate multidimensional features and classifiers in multiple end-to-end layers. Consequently, the deeper the network structure, the richer the feature level. However, the network can cause problems such as: 1) gradient disappearance; 2) gradient explosion; and 3) network degradation. To solve these problems, ResNet [53] was proposed, effectively mitigating network degradation and allowing more profound training of DLs through residual blocks. Zhao et al. [54] used SAR images to classify buildings, vegetation, roads, and water bodies using TerraSAR images [55]. Other approaches, such as those of Xing et al. [56] and Tavus et al. [57], use the U-Net architecture [58]. Katyar et al. [59] use the Sen1Floods11 dataset with SegNet [60]. Notably, U-Net uses skip connections between different blocks of each stage to preserve the acquired feature maps. At the same time, SegNet reuses the encoder's pooling indices for nonlinear upsampling, thus improving the results in flood detection. Bai et al. [61] improved on the work using BASNet [62], an image segmentation network identical to U-Net; they combined it with a hybrid loss function (structural similarity loss), intersection over union (IoU) loss, and focal loss.

On the other hand, Scepanovic et al. [63] created a land cover mapping system with five classes. They applied several semantic segmentation models such as U-Net, DeepLabV3+ [64], PSPNet [65], BiSeNet [66], SegNet, FCDenseNet [67], and FRRN-B [68]. Other approaches explore using self-supervised and semisupervised learning based on SimCLR [69] and FixMatch [70] to segment land use and flood mapping via Sen1Floods11.

Some RNN approaches have also been proposed for analyzing water bodies and land cover using Sentinel images [71], [72].

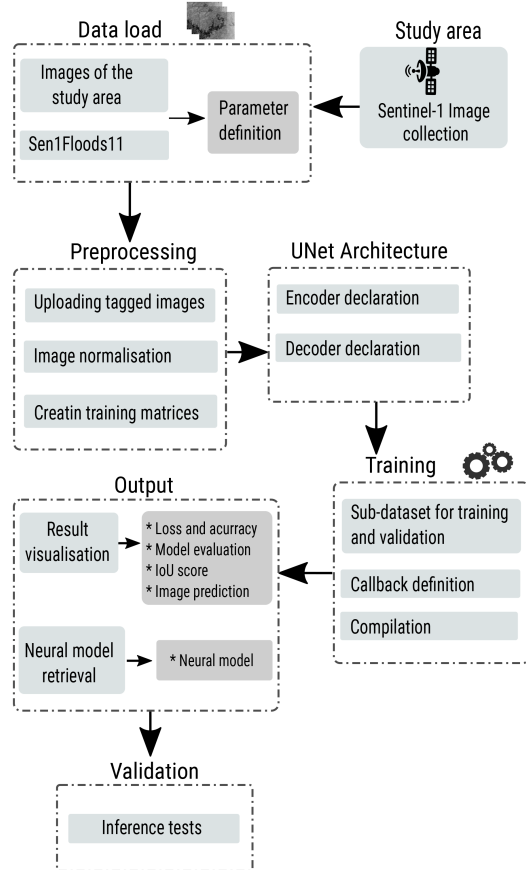


Fig. 3. Proposed architecture for flood segmentation.

In [73], [74], and [75], they proposed approaches incorporating recurrent and convolutional operations for treating spatiotemporal data. Contrastive learning [76] has recently emerged to avoid reliance on labeled data for flood mapping [22], [76], [77], [78].

III. METHODOLOGY FOR FLOOD SEGMENTATION IN SAR IMAGES

Satellite images have become a fundamental tool for understanding and mitigating the impact of natural disasters. The proposed methodology uses SAR images captured by the Sentinel-1 satellite to detect and segment floods. The U-Net neural network architecture identifies patterns and characteristics that differentiate flooded and nonflooded areas. The methodology can be seen in Fig. 3 and consists of a series of steps, which are explained as follows.

A. Study Area

The southeast of Mexico, Tabasco, was selected as the study area. Tabasco is located on the coast of the Gulf of Mexico. Its territorial extension is 24 661 km², representing 1.3% of the country. Two regions are recognized in the entity: Grijalva and Usumacinta, which contain two subregions (swamps and rivers). Together, they form one of the largest river systems in the world in terms of volume. In addition, the state's average precipitation is three times higher than the average in Mexico, representing

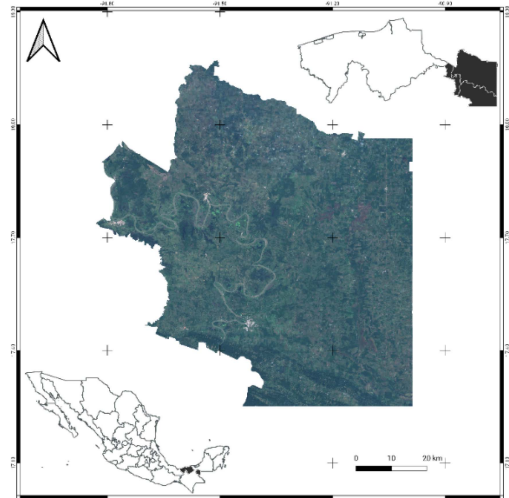


Fig. 4. Geographic location of the study area—Ríos subregion, Tabasco, Mexico.

almost 40% of the country's fresh water. The abundance of water and the impact of dams on the hydrology of the region, by altering the natural flow of rivers, cause flash floods and floods, which affect drinking water, health, and the livelihoods of thousands of Tabasco residents [79]. Therefore, flooding is expected in the region. However, in the fall of 2020, several river fronts and hurricanes caused the worst flooding in decades, causing human and economic losses. The study area focuses on the Ríos subregion (see Fig. 4). It is in the easternmost part of the state, on the borders of Campeche and the Republic of Guatemala. This is because of the many rivers that cross it, including the Usumacinta River, the largest in the country, and the San Pedro Mártir River. The municipalities that make up this subregion are Tenosique, Emiliano Zapata, and Balancán. Its surface is approximately 6000 km², representing 24.67% of the state's total.

SAR images with identical polarization in the return wave, horizontal–horizontal (HH) obtained from the Sentinel-1 satellite, were obtained using the Copernicus Open Access Hub¹ platform. The images are found within a tile that covered the states of Campeche, Chiapas, and Tabasco (see Fig. 5). Given that the study area has a large amount of vegetation, it was decided to use HH polarization since it has greater penetration through the canopy.

B. Load Data

This stage focuses on data acquisition and organization. Images of the study area and labels corresponding to the floods are collected for subsequent processing and model training. The Sen1Floods11 dataset is used to learn the neural network.

Sen1Floods11 [23] was created to train DL algorithms for flood detection; the type of calibration used is Beta nought. It covers 11 flood events (see Fig. 6) distributed in 14 biomes, 357 ecoregions, and six continents worldwide. It comprises 4831

¹<https://scihub.copernicus.eu/>

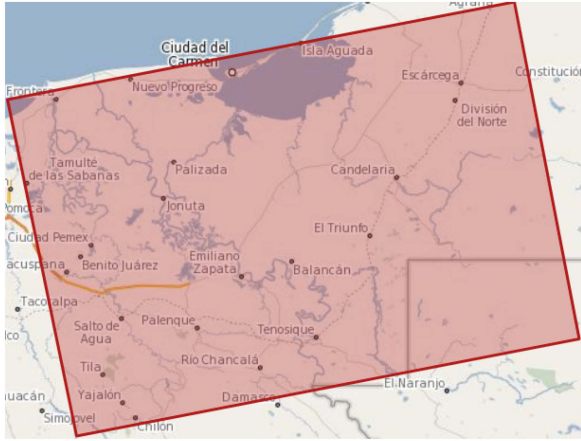


Fig. 5. Tile location containing the SAR images of the study.



Fig. 6. Geographic points where flood data were collected for Sen1Floods11.

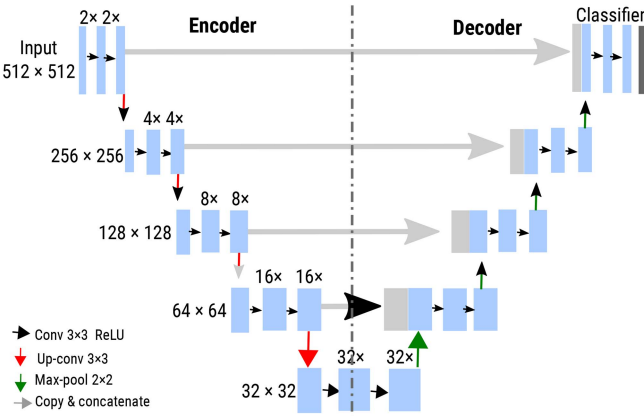


Fig. 7. Schematic of a U-Net architecture that receives as input a 512×512 pixel image with three channels.

image chips with a size of 512×512 pixels, covering a total area of $120\,406 \text{ km}^2$. Sentinel-1 images consist of two bands, vertical–vertical (VV) and vertical–horizontal (VH), representing backscatter values. Sentinel-2 images include 13 bands, all of which are TOA (below atmosphere atmospherically corrected images) reflectance values.

1) *Parameter Definition:* Some parameters were considered for our model.

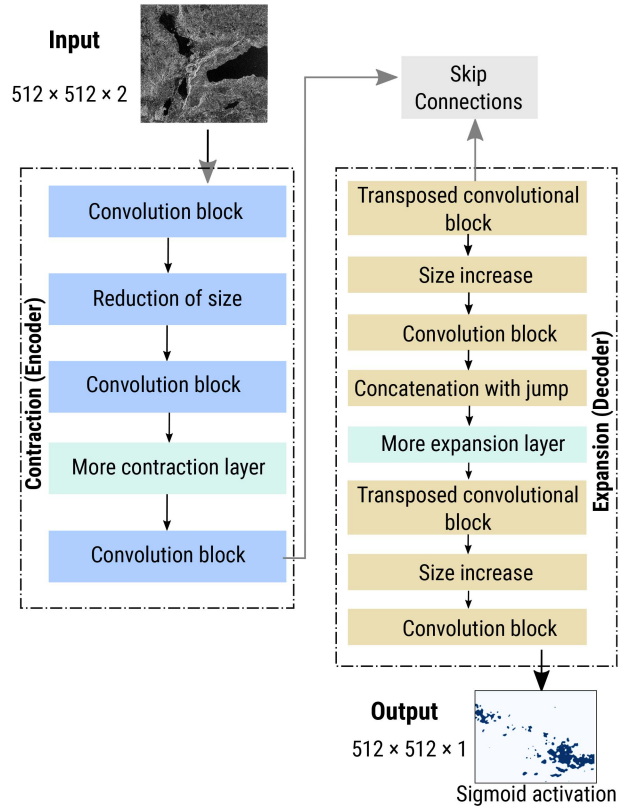


Fig. 8. General graphical scheme of the U-Net architecture used for the detection and segmentation of flooded areas in SAR images.

- Size of input images:* This parameter sets the size of the images in the dataset that would feed the neural model. This is important to ensure optimal performance in flood detection and segmentation. The declared size for the input images is 512×512 pixels to identify specific characteristics associated with flooding. The image size seeks to balance the need to capture relevant details in SAR images with the computational efficiency of the model.
- Bands to use from the input images:* In SAR imaging, channels relate to the different polarization bands in the images. The images generated by Sentinel-1 have two polarization bands: VV and VH. Each band represents unique information and characteristics inherent to the acquisition process and the interactions between electromagnetic waves and the observed terrain. The two bands were selected for primary model training because they capture distinct terrain properties: VV is sensitive to surface structure and roughness, including features such as vegetation, and VH is sensitive to the humidity and volume of objects, such as water on the ground. Combining both bands provides a complete and more detailed picture of the observed surface.
- Input layers:* The input layer is adjusted to the size of the established images of 512×512 . This layer provides a structure for entering data into the model and ensures that images are transformed and processed consistently according to the settings in each subsequent layer.

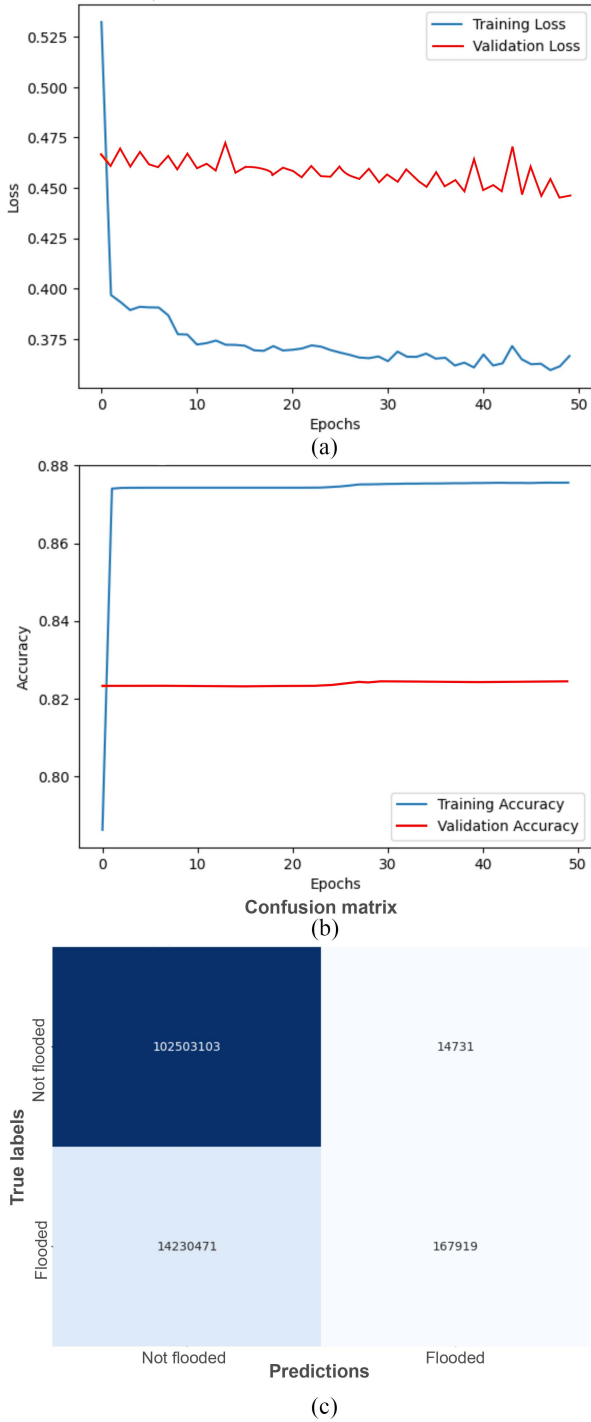


Fig. 9. Performance of the model with 50 epochs. (a) Loss in training. (b) Precision and validation. (c) Confusion matrix.

C. Preprocessing

In this phase, the images and masks of the Sen1Floods11 dataset are preprocessed to be entered into the neural model later. Among the challenges of SAR images is processing. This is due to the geometry of its acquisition, which generates geometric and radiometric deformation effects such as *slant range distortion*, *layover*, and *foreshortening* [80]. Warping effects can affect the

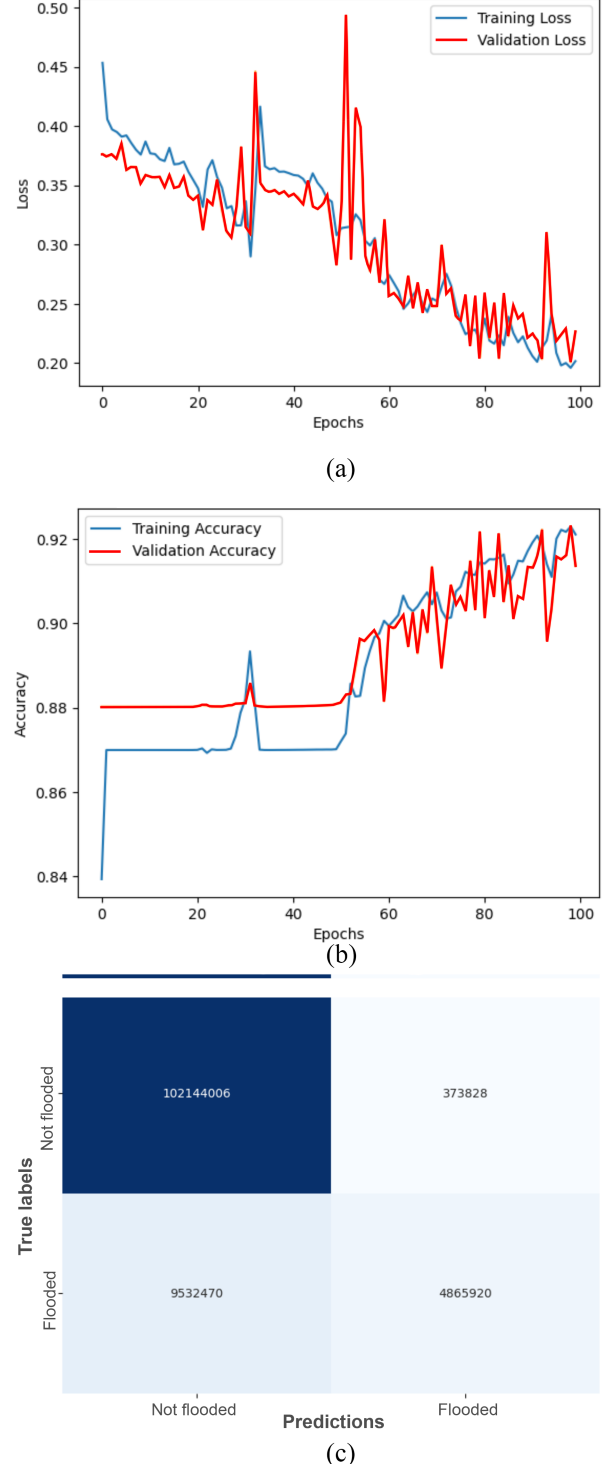
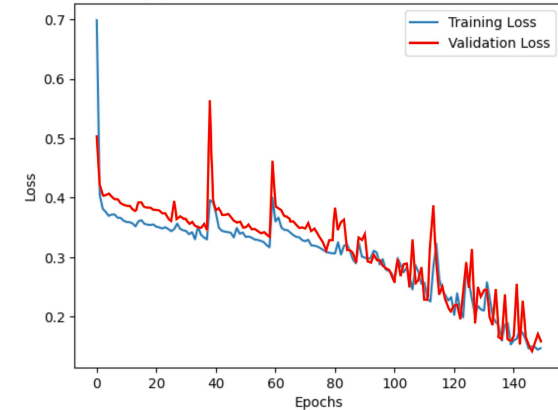
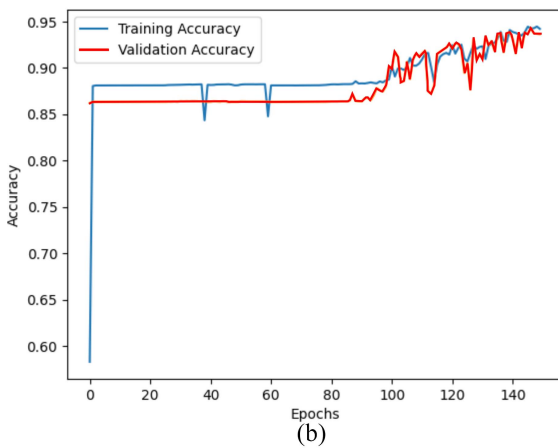


Fig. 10. Performance of the model with 100 epochs. (a) Loss in training. (b) Precision and validation. (c) Confusion matrix.

backscatter values of images. Loading images in TIF format begins with preprocessing to adapt them to the format required by the model. A transformation ensures that the images have the dimensions defined in the previous step. In addition, a transposition of the images is performed to adjust their channels to match the dimensions of the channels required by the



(a)



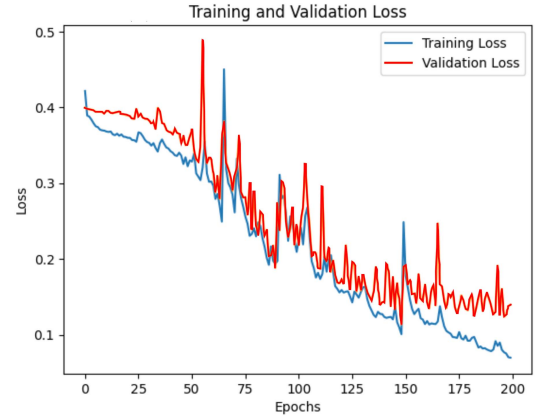
(b)



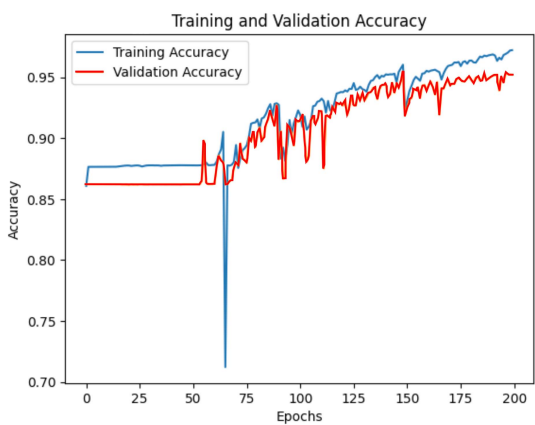
(c)

Fig. 11. Performance of the model with 150 epochs. (a) Loss in training. (b) Precision and validation. (c) Confusion matrix.

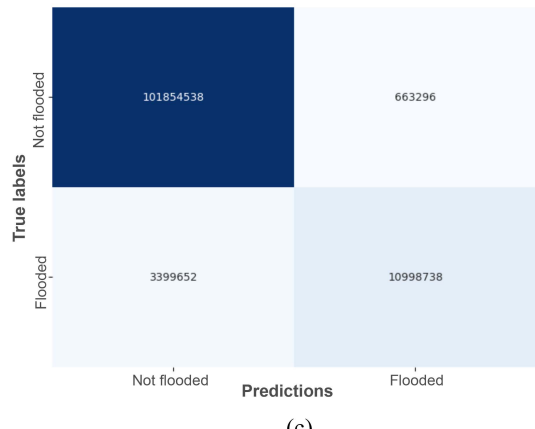
model. Radiometric calibration, terrain correction, and thermal noise elimination are performed in preprocessing. Backscatter coefficients are converted to decibels. VV + VH dual-band scenes acquired by Interferometric Wide swath are recovered. The scenes are then filtered according to the ascending and descending passes due to the influence of the angle of incidence on the backscatter coefficient. Channels VV and VH are clipped within the range of $(-23, 0)$ dB for VV and $(-28, -5)$ dB for VH. Subsequently, the pixel intensity values are normalized.



(a)



(b)



(c)

Fig. 12. Performance of the model with 200 epochs. (a) Loss in training. (b) Precision and validation. (c) Confusion matrix.

Normalization is a fundamental step in standardizing the scale of the data and ensuring that the values are within a range that facilitates the training of the neural model. Normalization is performed by dividing the pixel intensity values by 255, which will scale the values to 0 and 1: 1 for pixels corresponding to floods and 0 in nonflooded areas.

They are creating matrices for training houses the preprocessed images and their respective flood reference masks. The matrices X and Y are created. The masks are represented in binary format: 1 for flooded and 0 for nonflooded areas.

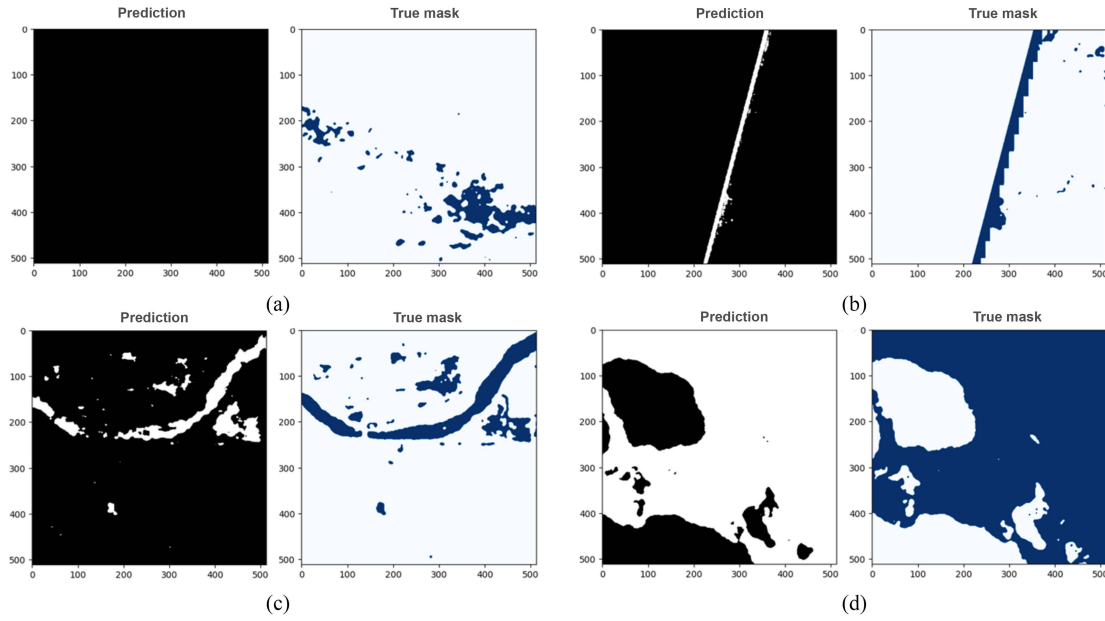


Fig. 13. Results of the visualization of the segmentation. Right, ground truth. Left, model predictions. (a) 50 epochs. (b) 100 epochs. (c) 150 epochs. (d) 200 epochs.

D. U-Net Architecture

The U-Net architecture is a CNN designed for image segmentation. It can learn specific features in images by combining low-level and high-level features. Despite being one of the simplest models, it offers more precise or adjusted results than other models (see Fig. 7). The accuracy is due to its handling of small datasets [58].

The creation of the U-Net architecture for the detection and segmentation of flooded areas consists of two main parts (see Fig. 8): the contraction path (encoder) and the expansion path (decoder). Jump connections interconnect both. Furthermore, it ends in an output layer, which generates the segmented mask of the areas of interest.

E. Training

Essential aspects for training were configured to compile the model. The Adam optimization algorithm was used. Adam combines the advantages of RMSprop and Momentum to improve the model learning process [81]. Both use the history of previous gradients to update the model parameters. However, instead of a constant learning rate, it adjusts the rate of each parameter individually based on its estimate of the Momentum and magnitude of the gradient. This allows for more efficient and accurate fitting to the training data, resulting in more excellent prediction accuracy than other optimization methods. Binary cross-entropy [82] was used as the loss function, which is generally used in binary classification problems but also in problems where the variables to be predicted take values between 0 and 1.

- 1) *Subdataset for training and validation:* Manually labeled Sen1Floods11 data are divided into subsets to train, validate, and test the model. These manually labeled data are Sentinel-1 SAR images that expert remote sensing analysts have labeled to indicate the presence or absence

of flooding in each pixel. Three subsets were made: a) model training set (70% of the dataset); b) validation set (15% of the dataset) to tune the model hyperparameters and prevent overfitting; and c) test set (15% of the dataset), data to evaluate the model and provide a realistic estimate of its performance.

- 2) *Definition of callbacks:* Callbacks were implemented to control the training process and make decisions based on the model's performance. One of the most critical Callbacks is Model Checkpoint, which saves the model with the lowest loss to the validation set during training. In addition, the Early Stopping parameter was used to stop model training if no improvement in validation loss was observed for a specific number of epochs (in this case, 70 epochs).

The model was trained and validated using the subsets for these purposes. A batch size of 32 images per iteration was used during training. Different training tests were performed with different numbers of epochs (50, 100, 150, and 200) to evaluate performance over time. This allowed us to determine with how many epochs the best results are obtained regarding loss and precision in the validation set. Training was performed by iterating through the training batches at each iteration. Model weights are updated to minimize the loss function. Training progress is monitored, and loss and accuracy are recorded at each training and validation set epoch.

F. Output

- 1) *Viewing Results:* In this phase, metrics and visualizations that allow us to understand the performance and effectiveness of the model in detecting and segmenting floods in SAR images are obtained. It ranges from the evaluation of the quality of the

training to the application of the model. The main components are detailed as follows.

- 1) *Loss and precision to understand how the model adapts to the data and training over time:* These metrics provide information about model convergence and whether overfitting or underfitting occurs. A gradual decrease in loss and an increase in accuracy indicate successful training.
- 2) *Model evaluation:* The test subset is used to evaluate the model's actual performance. The model predictions are applied to these images and compared to the flood masks. This allows various evaluation metrics to be calculated, such as precision, recall, and IoU score.
- 3) *IoU score calculation to evaluate the quality of the segmentation:* This is calculated by dividing the intersection area between the predicted mask and the actual mask by the area of their union. Higher IoU indicates higher overlap and accuracy in predicting flooded areas.
- 4) *Prediction on test images, applied to a test image to generate a prediction of the flooded areas:* This prediction is visually compared to the actual flood mask in the same image to evaluate the accuracy and quality of the segmentation. Detected and actual areas can be overlaid to analyze coincidences and deviations.

G. Validation

An inference test is performed to predict new flood images obtained from SAR images. In this phase, the knowledge acquired during model training is applied to detect flooded areas in real-world scenarios. The key components are described as follows.

- 1) *Loading of the trained neural model:* It contains the weights and architecture learned during the training process for classifying flooded areas.
- 2) *Preprocess and postprocess:* Preprocessing functions are used to prepare the images properly, including normalizing pixel values and adjusting the size to match the model input format. After obtaining model predictions, postprocessing functions are used to improve and refine the outputs. This could involve removing small groups of unwanted pixels and improving the consistency of segmented areas.
- 3) *New image classification:* Classification proceeds once the image has been preprocessed and the model loaded. The image is input into the model, and predictions are generated about the areas that could be flooded. The model uses its prior understanding of patterns learned during training to make these predictions.
- 4) *Visualization of results:* The model predictions can be visualized by overlaying them on the original image. This allows a visual assessment of how the model has identified flooded areas compared to reality. The overlay can also indicate the quality of the segmentation and whether there are areas for improvement.

IV. RESULTS OBTAINED

A. Model Evaluation Metrics

The following metrics were selected to evaluate the developed neural model: loss, recall, precision, F1-score, accuracy, confusion matrix, and IoU [83], [84].

- 1) *Loss:* It is a metric that quantifies the difference between model predictions and actual labels. A more minor loss indicates better agreement between model predictions and labels. The loss was evaluated at different training epochs (50, 100, 150, and 200) to understand the evolution and convergence to a minimum value for better fitting the data.
- 2) *Recall:* It measures the proportion of positive instances (flooded areas) the model correctly identified compared to the total number of positive instances. A high recall indicates the model's ability to detect most flooded areas in the SAR image.
- 3) *Precision:* It measures the fraction correctly detected by the model.
- 4) *F1-score:* It is a metric that combines the precision and recall of the model. It measures the ratio between true and false positive predictions compared to the actual labels. It is advantageous when there is an imbalance between classes, such as in segmenting flooded areas where non-flooded areas are predominant.
- 5) *Accuracy:* It evaluates the overall accuracy of a classifier. It indicates the overall performance of the model.
- 6) *Confusion matrix:* This shows the number of valid, false positives, true negatives, and false negatives in the model classification.
- 7) *IoU:* It measures the overlap between the segmentation masks generated by the model and the ground truth masks.

These metrics were evaluated in different training epochs: 50, 100, 150, and 200. The model's improvement can be observed throughout each epoch and the equilibrium points where performance stabilizes. In addition, it allows for identifying the stage where the model achieves an optimal balance between precision and recall.

Training the neural network with 50 epochs reached a loss level of 0.3666 and 0.4462 on the validation set [see Fig. 9(a)]. The loss in training indicates the magnitude of the difference between the model predictions and the actual labels. The increase in loss on the validation set is because the model was overfitting. The accuracy achieved in the training set was 0.8756, and on the validation set, it was 0.8244 [see Fig. 9(b)]. This indicates that 87.56% of the model predictions match the actual labels in the training set. Although the model shows excellent predictive ability in the training set, its performance in validation is slightly lower. The F1-score was 0.0230 in the test set, indicating that the model balances accuracy and can detect true positives. However, it is essential to note that the low F1-value is due to the imbalance in the flooded and nonflooded classes in the test set. It is worth mentioning that the terrain characteristics and the angle of incidence of the image produce areas with excessive shadowing; this causes the model to detect false positives from areas with flooding present.

TABLE I
RESULTS OF THE METRICS USED TO EVALUATE THE PERFORMANCE OF THE U-NET MODEL TRAINED AT 50 EPOCHS

Metrics	Decimal	Percent
Loss	0.4462	44.62%
Accuracy	0.8244	82.44%
F1-Score	0.0230	2.3 %
Recall	0.0117	1.17%
Precision	0.9193	91.93%
IoU	0.0117	1.17%

TABLE II
RESULTS OF THE METRICS USED TO EVALUATE THE PERFORMANCE OF THE U-NET MODEL TRAINED AT 100 EPOCHS

Metrics	Decimal	Percent
Loss	0.2267	22.67%
Accuracy	0.9137	91.37%
F1-Score	0.4956	49.56%
Recall	0.3379	33.79%
Precision	0.9287	92.87%
IoU	0.3294	32.94%

The recall had a value of 0.0117, indicating that the model has difficulty detecting most of the flooded areas in the image. This is due to the limitation of the model with 50-epoch training. The precision, which measures the model's ability to identify flooded areas correctly, was 0.9193. This means that the model positively predicts 91.93% of the flooded areas. The confusion matrix shows that the model classified 1.16% as true positives (167 919 instances), 0.01% as false positives (14 731 instances), and 99.99% as true negatives (102 503 103 instances); however, it classified 98.84% (14 230 471 instances) false negatives [see Fig. 9(c)]. The IoU score was 0.0117. This value reflects the model's ability to perform accurate segmentation and coincides with the low recall value observed.

The above results suggest that the model trained with 50 epochs has limitations in detecting and segmenting flooded areas in SAR images. Although it shows acceptable precision, its recall and IoU are low. Table I presents a summary of the results obtained.

Training the model with 100 epochs reached a loss value on the training set of 0.2017, thus reducing the discrepancy between predictions and labels; the loss on the validation set was 0.2267 [see Fig. 10(a)]. The accuracy in the training set was 0.9211, which means that the model correctly classified 92.11% of the instances; on the validation set, the precision was 0.9137, slightly lower but significant [see Fig. 10(b)]. The F1-score value was 0.4956, which shows the ability of the model to find a balance in identifying flooded and nonflooded areas. The recall reached a value of 0.3379, detecting a third of the flooded areas. The precision was 0.9287, indicating that 92.87% of the predicted instances correspond to the flooded areas. The confusion matrix correctly identified 91.46% of nonflooded areas (102 144 006 instances) and 92.87% of flooded areas (4 865 920 instances). However, it misclassified 8.52% as flooded areas (9 532 470 instances) and 7.12% (373 828 instances) as nonflooded areas [see Fig. 10(c)]. The IoU score was 0.3294, indicating a significant correlation between the areas identified by the model and

TABLE III
RESULTS OF THE METRICS USED TO EVALUATE THE PERFORMANCE OF THE U-NET MODEL TRAINED AT 150 EPOCHS

Metrics	Decimal	Percent
Loss	0.1467	14.67%
Accuracy	0.9363	93.63%
F1-Score	0.7874	78.74%
Recall	0.7718	77.18%
Precision	0.8037	80.37%
IoU	0.6494	64.94%

the actual flooding areas. Table II presents a summary of the obtained results.

They are training with 150 epochs to achieve promising and robust performance in flooded area segmentation. Its loss was 0.1467, which suggests that the model has managed to minimize the discrepancy between its predictions and the actual labels [see Fig. 11(a)]. The overall accuracy reaches a solid 0.9420 on the training set, showing that the model can perform accurate classification in most instances. The validation set's accuracy remains at a satisfactory level of 0.9363 [see Fig. 11(b)]. F1-score had a value of 0.7874, demonstrating that the model balances precision and recall when considering both true positives and false positives and false negatives. Recall performed well, with a solid value of 0.7718. The precision was 0.8037, which avoids false positives and performs adequate segmentations. The matrix shows that the model improved its performance; it classified 97.34% of instances as non-flooded areas (99 802 794 instances) and 77.17% as flooded areas (11 112 871 instances). However, 2.64% of misclassified cases were identified as false positives (2 715 040 instances), and 22.83% (3 285 519) were misclassified as false negatives [see Fig. 11(c)]. The model obtains an IoU score of 0.6494, meaning that there is a significant overlap between the areas segmented by the model and the actual flooded areas. In Table III, the summary of the results obtained is presented.

Training with 200 epochs achieved a loss of 0.0697 and, during validation, a loss of 0.1396, indicating that the model has achieved excellent agreement between predictions and accurate labels during training [see Fig. 12(a)]. The accuracy was 0.9519 [see Fig. 12(b)], demonstrating that the model effectively generalized the relationships learned during training to new data. F1-score obtained 0.8441 and recall 0.7639. The precision was 0.9431, underlining the model's reliability in classifying flooded areas. The matrix shows high model performance, with 99.35% (101 854 538 instances) as nonflooded areas correctly identified and 76.39% as flooded areas (10 998 738 instances), 0.65% incorrectly classified as flooded areas (663 296 instances) and 23.60% (3 399 652 instances) of areas wrongly flooded [see Fig. 12(c)]. Finally, the IoU score was 0.7302. Table IV presents a summary of the results obtained.

B. Visualization of Segmentations

Fig. 13 shows the results of the segmentation tests. On the left side, you can see the prediction made by the model. Areas that the model identifies as flooded are highlighted in white. Overlaying the blank segmented areas with the actual flooded

TABLE IV
RESULTS OF THE METRICS USED TO EVALUATE THE PERFORMANCE OF THE U-NET MODEL TRAINED AT 200 EPOCHS

Metrics	Decimal	Percent
Loss	0.1396	13.96%
Accuracy	0.9519	95.19%
F1-Score	0.8441	84.41%
Recall	0.7639	76.39%
Precision	0.9431	94.31%
IoU	0.7302	73.02%

areas provides a visual assessment of the accuracy of the model predictions. On the right side is the ground truth mask used for the model input, where flooded areas are marked in blue.

As shown in Fig. 13(a), segmentation with 50 epochs needs to be revised. The IoU score was 1.17% and accuracy was 91.93% (see Table I). The model achieves significant segmentation skills with 100 epochs [see Fig. 13(b)]. As evidence, its IoU score is 32.94% and accuracy is 92.87% (see Table II). Tests conducted with 150 epochs [see Fig. 13(c)] highlight the model's ability to identify flooded areas and achieve segmentation that overlaps significantly with the actual flooded areas. The IoU score was 64.94% and accuracy was 80.73% (see Table III). The training with 200 epochs obtained the best results, with an IoU score of 73.02% and accuracy of 94.31% (see Table IV). These visualizations provide a concrete graphical representation of how the model identifies and segments flooded areas in SAR imagery.

V. CONCLUSION

The segmentation model based on the U-Net architecture effectively identifies flooded areas. The ability of U-Net to capture relevant features in SAR images and its training and validation are reflected in the obtained results. The tests with 200 epochs obtained the best results with an IoU score of 73.02% and accuracy of 94.31%.

Despite the achievements made, several paths could be explored in future works further to improve flood detection and segmentation in SAR images.

- 1) *Architecture improvement:* Use other architectures such as DeepLab and PSPNet that could be considered to explore new feature extraction capabilities.
- 2) *Parameter optimization:* Although tests have been performed to determine the optimal number of training epochs, more profound optimization can be performed to fine-tune the hyperparameters and achieve a balance between accuracy and training time.
- 3) *Use of multitemporal data:* Integrating multitemporal data from different satellites could allow better flood detection by considering the temporal evolution of the affected areas.

As challenges are addressed and new opportunities are explored, this methodology will likely continue to improve and significantly impact disaster management and data-driven decision making.

REFERENCES

- [1] CRED, “2021 disasters in numbers,” Centre Res. Epidemiol. Disasters, Brussels, Belgium, Tech. Rep., 2021. [Online]. Available: https://cred.be/sites/default/files/2021_EMDAT_report.pdf
- [2] D. Tin, L. Cheng, D. Le, R. Hata, and G. Ciottone, “Natural disasters: A comprehensive study using EMDAT database 1995–2022,” *Public Health*, vol. 226, pp. 255–260, 2024.
- [3] E. Psomiadis, “Flash flood area mapping utilising SENTINEL-1 radar data,” *Proc. SPIE*, 2016, vol. 10005, Art. no. 100051G.
- [4] P. Wallemacq and R. House, “Economic losses, poverty and disasters (1998–2017),” Centre for Research on the Epidemiology of Disasters United Nations Office for Disaster Risk Reduction, Tech. Rep., 2018. [Online]. Available: https://www.preventionweb.net/files/61119_credeconomiclosses.pdf
- [5] F. Pech-May, R. Aquino-Santos, G. Rios-Toledo, and J. P. F. Posadas-Durán, “Mapping of land cover with optical images, supervised algorithms, and Google earth engine,” *Sensors*, vol. 22, no. 13, 2022, Art. no. 4729.
- [6] E. Benami et al., “Uniting remote sensing, crop modelling and economics for agricultural risk management,” *Nature Rev. Earth Environ.*, vol. 2, pp. 1–20, 2021.
- [7] J. Paz, F. Jiménez, and B. Sánchez, “Urge manejo del agua en tabasco,” Universidad Nacional Autónoma de México y Asociación Mexicana de Ciencias para el Desarrollo Regional A.C., Ciudad de México, Mexico, Tech. Rep., 2018.
- [8] CEPAL, “Tabasco: Características e impacto socioeconómico de las inundaciones provocadas a finales de octubre y a comienzos de noviembre de 2007 por el frente frío número 4,” Comisión Económica para América Latina y el Caribe Sede Subregional en México, Mexico City, México, Tech. Rep., 2008. [Online]. Available: <https://hdl.handle.net/11362/25881>
- [9] J. Cuevas, M. F. Enriquez, and R. Norton, “Tabasco floods of 2020—Learning from the past to prepare for the future,” ISET International and the Zurich Flood Resilience Alliance, Boulder, CO, USA, Tech. Rep., 2022. [Online]. Available: https://preparecenter.org/wp-content/uploads/2023/03/PERC-fullreport_Mexico_ENG.pdf
- [10] M. Perevochtchikova and J. Torre, “Causas de un desastre: Inundaciones del 2007 en tabasco, México,” *J. Latin Amer. Geography*, vol. 9, pp. 73–98, 2010.
- [11] G. J.-P. Schumann and D. K. Moller, “Microwave remote sensing of flood inundation,” *Phys. Chem. Earth, Parts A/B/C*, vol. 83–84, pp. 84–95, 2015.
- [12] W. Emery and A. Camps, “The history of satellite remote sensing,” in *Introduction to Satellite Remote Sensing*, W. Emery and A. Camps, Eds., New York, NY, USA: Springer, 2017, pp. 1–42.
- [13] T. M. Lillesand, *Remote Sensing and Image Interpretation*. Hoboken, NJ, USA: Wiley, 2006.
- [14] S. Jutz and M. Milagro-Pérez, “1.06—Copernicus program,” in *Comprehensive Remote Sensing*, S. Liang, Ed., Amsterdam, The Netherlands: Elsevier, 2018, pp. 150–191.
- [15] A. Twele, W. Cao, S. Plank, and S. Martinis, “Sentinel-1-based flood mapping: A fully automated processing chain,” *Int. J. Remote Sens.*, vol. 37, no. 13, pp. 2990–3004, 2016.
- [16] M. Chini, R. Pelich, L. Pulvirenti, N. Pierdicca, R. Hostache, and P. Matgen, “Sentinel-1 InSAR coherence to detect floodwater in urban areas: Houston and hurricane Harvey as a test case,” *Remote Sens.*, vol. 11, no. 2, 2019, Art. no. 107.
- [17] K. K. Singh and A. Singh, “Identification of flooded area from satellite images using Hybrid Kohonen Fuzzy C-means sigma classifier,” *Egyptian J. Remote Sens. Space Sci.*, vol. 20, no. 1, pp. 147–155, 2017.
- [18] V. Lalitha and B. Latha, “A review on remote sensing imagery augmentation using deep learning,” *Mater. Today: Proc.*, vol. 62, pp. 4772–4778, 2022.
- [19] L. Alzubaidi, J. Zhang, A. J. Humaidi, and A. Al-Dujaili, “Review of deep learning: Concepts, CNN architectures, challenges, applications, future directions,” *J. Big Data*, vol. 53, no. 8, pp. 1–74, 2021.
- [20] I. Goodfellow, Y. Bengio, and A. Courville, *Deep Learning*. Cambridge, MA, USA: MIT Press, 2016.
- [21] R. Bentivoglio, E. Isufi, S. N. Jonkman, and R. Taormina, “Deep learning methods for flood mapping: A review of existing applications and future research directions,” *Hydrol. Earth Syst. Sci.*, vol. 26, no. 16, pp. 4345–4378, 2022.
- [22] C. P. Patel, S. Sharma, and V. Gulshan, “Evaluating self and semi-supervised methods for remote sensing segmentation tasks,” *CoRR*, vol. abs/2111.10079, 2021. [Online]. Available: <https://dblp.unitrier.de/rec/journals/corr/abs-2111-10079.html?view=bibtex>

- [23] D. Bonafilia, B. Tellman, T. Anderson, and E. Issenberg, "Sen1Floods11: A georeferenced dataset to train and test deep learning flood algorithms for sentinel-1," in *Proc. IEEE/CVF Conf. Comput. Vis. Pattern Recognit. Workshops*, 2020, pp. 835–845.
- [24] UNOSAT, "Unosat flood dataset," 2019. Accessed: Jun. 20, 2022. [Online]. Available: <http://floods.unosat.org/geoportal/catalog/main/home.page>
- [25] G. I. Drakonakis, G. Tsagkatakis, K. Fotiadou, and P. Tsakalides, "OmbriaNet—Supervised flood mapping via convolutional neural networks using multitemporal Sentinel-1 and Sentinel-2 data fusion," *IEEE J. Sel. Topics Appl. Earth Observ. Remote Sens.*, vol. 15, pp. 2341–2356, 2022.
- [26] C. Rambour, N. Audebert, E. Koeniguer, B. Le Saux, M. Crucianu, and M. Datcu, "SEN12-FLOOD: A SAR and multispectral dataset for flood detection," 2020, doi: [10.21227/w6xz-s898](https://doi.org/10.21227/w6xz-s898).
- [27] V. Tsyganskaya, S. Martinis, P. Marzahn, and R. Ludwig, "SAR-based detection of flooded vegetation—A review of characteristics and approaches," *Int. J. Remote Sens.*, vol. 39, no. 8, pp. 2255–2293, 2018.
- [28] C. Rambour, N. Audebert, E. Koeniguer, B. Le Saux, M. Crucianu, and M. Datcu, "Flood detection in time series of optical and SAR images," in *Proc. Int. Arch. Photogrammetry, Remote Sens. Spatial Inf. Sci.*, 2020, pp. 1343–1346.
- [29] G. Mateo-Garcia et al., "Towards global flood mapping onboard low cost satellites with machine learning," *Sci. Rep.*, vol. 11, no. 1, 2021, Art. no. 7249.
- [30] S. Grimaldi, Y. Li, V. Pauwels, and J. Walker, "Remote sensing-derived water extent and level to constrain hydraulic flood forecasting models: Opportunities and challenges," *Surv. Geophys.*, vol. 37, no. 5, pp. 977–1034, 2016.
- [31] X. Shen, D. Wang, K. Mao, E. Anagnostou, and Y. Hong, "Inundation extent mapping by synthetic aperture radar: A review," *Remote Sens.*, vol. 11, no. 7, 2019, Art. no. 879.
- [32] M. V. Bernhofen et al., "The role of global data sets for riverine flood risk management at national scales," *Water Resour. Res.*, vol. 58, no. 4, 2022, Art. no. e2021WR031555.
- [33] R. Sadiq, M. Imran, and F. Ofli, *Remote Sensing for Flood Mapping and Monitoring*. Singapore: Springer, 2023, pp. 679–697.
- [34] J. Yu, Z. Wang, V. Vasudevan, L. Yeung, M. Seyedhosseini, and Y. Wu, "CoCa: Contrastive captioners are image-text foundation models," 2022, [arXiv:2205.01917](https://arxiv.org/abs/2205.01917).
- [35] J. Rosentreter, R. Hagensieker, and B. Waske, "Towards large-scale mapping of local climate zones using multitemporal Sentinel 2 data and convolutional neural networks," *Remote Sens. Environ.*, vol. 237, 2020, Art. no. 111472.
- [36] S. Martinis, S. Groth, M. Wieland, L. Knopp, and M. Rättich, "Towards a global seasonal and permanent reference water product from Sentinel-1/2 data for improved flood mapping," *Remote Sens. Environ.*, vol. 278, 2022, Art. no. 113077.
- [37] Z. Gou, "Urban road flooding detection system based on SVM algorithm," in *Proc. 2nd Int. Conf. Mach. Learn. Comput. Appl.*, 2021, pp. 1–8.
- [38] A. H. Tanim, C. B. McRae, H. Tavakol-Davani, and E. Goharian, "Flood detection in urban areas using satellite imagery and machine learning," *Water*, vol. 14, no. 7, 2022, Art. no. 1140.
- [39] K. Kunverji, K. Shah, and N. Shah, "A flood prediction system developed using various machine learning algorithms," *Proc. 4th Int. Conf. Adv. Sci. Technol.*, 2021. [Online]. Available: https://papers.ssrn.com/sol3/papers.cfm?abstract_id=3866524
- [40] C. Alexander, "Normalized difference spectral indices and urban land cover as indicators of land surface temperature (1st)," *Int. J. Appl. Earth Observ. Geoinf.*, vol. 86, 2020, Art. no. 102013.
- [41] V. Kumar, A. Sharma, R. Bhardwaj, and A. K. Thukral, "Comparison of different reflectance indices for vegetation analysis using Landsat-TM data," *Remote Sens. Appl.: Soc. Environ.*, vol. 12, pp. 70–77, 2018.
- [42] J. Campbell and R. Wynne, *Introduction to Remote Sensing*, 5th ed. New York City, NY, USA: Guilford Publications, 2011.
- [43] J. Rouse, J. W., R. H. Haas, J. A. Schell, and D. W. Deering, "Monitoring vegetation systems in the great plains with ERTS," in *Proc. 3rd ERTS Symp.*, 1974, vol. 351, pp. 309–317.
- [44] G. Bo-cai, "NDWI—A normalized difference water index for remote sensing of vegetation liquid water from space," *Remote Sens. Environ.*, vol. 58, no. 3, pp. 257–266, 1996.
- [45] P. Deroliya, M. Ghosh, M. P. Mohanty, S. Ghosh, K. D. Rao, and S. Karmakar, "A novel flood risk mapping approach with machine learning considering geomorphic and socio-economic vulnerability dimensions," *Sci. Total Environ.*, vol. 851, 2022, Art. no. 158002.
- [46] Y. Zhou, J. Luo, Z. Shen, X. Hu, and H. Yang, "Multiscale water body extraction in urban environments from satellite images," *IEEE J. Sel. Topics Appl. Earth Observ. Remote Sens.*, vol. 7, no. 10, pp. 4301–4312, Oct. 2014.
- [47] M. G. Tulbure, M. Broich, S. V. Stehman, and A. Kommareddy, "Surface water extent dynamics from three decades of seasonally continuous Landsat time series at subcontinental scale in a semi-arid region," *Remote Sens. Environ.*, vol. 178, pp. 142–157, 2016.
- [48] G. Schumann, J. Henry, L. Hoffmann, L. Pfister, F. Pappenberger, and P. Matgen, "Demonstrating the high potential of remote sensing in hydraulic modelling and flood risk management," in *Proc. Annu. Conf. Remote Sens. Photogrammetry Soc. NERC Earth Observ. Conf.*, 2005, pp. 6–9.
- [49] N. Anusha and B. Bharathi, "Flood detection and flood mapping using multi-temporal synthetic aperture radar and optical data," *Egypt. J. Remote Sens. Space Sci.*, vol. 23, pp. 207–219, 2020.
- [50] G. Konapala, S. V. Kumar, and S. K. Ahmad, "Exploring Sentinel-1 and Sentinel-2 diversity for flood inundation mapping using deep learning," *ISPRS J. Photogrammetry Remote Sens.*, vol. 180, pp. 163–173, 2021.
- [51] T. G. J. Rudner et al., "Multi3Net: Segmenting flooded buildings via fusion of multiresolution, multisensor, and multitemporal satellite imagery," in *Proc. AAAI Conf. Artif. Intell.*, 2019, vol. 33, pp. 702–709.
- [52] Y. Li, S. Martinis, and M. Wieland, "Urban flood mapping with an active self-learning convolutional neural network based on TerraSAR-X intensity and interferometric coherence," *ISPRS J. Photogrammetry Remote Sens.*, vol. 152, pp. 178–191, 2019.
- [53] K. He, X. Zhang, S. Ren, and J. Sun, "Deep residual learning for image recognition," in *Proc. IEEE Conf. Comput. Vis. Pattern Recognit.*, 2016, pp. 770–778.
- [54] B. Zhao, H. Sui, C. Xu, and J. Liu, "Deep learning approach for flood detection using SAR image: A case study in Xinxiang," in *Proc. Int. Arch. Photogrammetry, Remote Sens. Spatial Inf. Sci.*, 2022, pp. 1197–1202.
- [55] J. Betbeder, S. Rapinel, T. Corpetti, E. Pottier, S. Corgne, and L. Hubert-Moy, "Multitemporal classification of TerraSAR-X data for wetland vegetation mapping," *J. Appl. Remote Sens.*, vol. 8, 2014, Art. no. 083648.
- [56] Z. Xing et al., "Flood vulnerability assessment of urban buildings based on integrating high-resolution remote sensing and street view images," *Sustain. Cities Soc.*, vol. 92, 2023, Art. no. 104467.
- [57] B. Tavus, R. Can, and S. Kocaman, "A CNN-based flood mapping approach using Sentinel-1 data," *ISPRS Ann. Photogrammetry, Remote Sens. Spatial Inf. Sci.*, vol. 3, pp. 549–556, 2022.
- [58] O. Ronneberger, P. Fischer, and T. Brox, "U-Net: Convolutional networks for biomedical image segmentation," in *Proc. Med. Image Comput. Computer-Assisted Interv.*, 2015, pp. 234–241.
- [59] V. Katiyar, N. Tamkuwan, and M. Nagai, "Near-real-time flood mapping using off-the-shelf models with SAR imagery and deep learning," *Remote Sens.*, vol. 13, no. 12, 2021, Art. no. 2334.
- [60] A. Moradi Sizkouhi, M. Aghaei, and S. M. Esmailifar, "A deep convolutional encoder-decoder architecture for autonomous fault detection of PV plants using multi-copters," *Sol. Energy*, vol. 223, pp. 217–228, 2021.
- [61] Y. Bai et al., "Enhancement of detecting permanent water and temporary water in flood disasters by fusing Sentinel-1 and Sentinel-2 imagery using deep learning algorithms: Demonstration of Sen1Floods11 benchmark datasets," *Remote Sens.*, vol. 13, no. 11, 2021, Art. no. 2220.
- [62] X. Qin, Z. Zhang, C. Huang, C. Gao, M. Dehghan, and M. Jagersand, "BASNet: Boundary-aware salient object detection," in *Proc. IEEE/CVF Conf. Comput. Vis. Pattern Recognit.*, 2019, pp. 7471–7481.
- [63] S. Scepanovic, O. Antropov, P. Laurila, Y. Rauste, V. Ignatenko, and J. Praks, "Wide-area land cover mapping with Sentinel-1 imagery using deep learning semantic segmentation models," *IEEE J. Sel. Topics Appl. Earth Observ. Remote Sens.*, vol. 14, pp. 10357–10374, 2021.
- [64] L.-C. Chen, Y. Zhu, G. Papandreou, F. Schroff, and H. Adam, "Encoder-decoder with atrous separable convolution for semantic image segmentation," in *Proc. Eur. Conf. Comput. Vis.*, 2018, pp. 801–818.
- [65] H. Zhao, J. Shi, X. Qi, X. Wang, and J. Jia, "Pyramid scene parsing network," in *Proc. IEEE Conf. Comput. Vis. Pattern Recognit.*, 2017, pp. 6230–6239.
- [66] C. Yu, J. Wang, C. Peng, C. Gao, G. Yu, and N. Sang, "BiSeNet: Bilateral segmentation network for real-time semantic segmentation," in *Proc. Eur. Conf. Comput. Vis.*, 2018, pp. 334–349.
- [67] S. Jégou, M. Drozdzal, D. Vazquez, A. Romero, and Y. Bengio, "The one hundred layers Tiramisu: Fully convolutional DenseNets for semantic segmentation," in *Proc. IEEE Conf. Comput. Vis. Pattern Recognit. Workshops*, 2017, pp. 11–19.

- [68] T. Pohlen, A. Hermans, M. Mathias, and B. Leibe, "Full-resolution residual networks for semantic segmentation in street scenes," in *Proc. IEEE Conf. Comput. Vis. Pattern Recognit.*, 2017, pp. 4151–4160.
- [69] T. Chen, S. Kornblith, M. Norouzi, and G. Hinton, "A simple framework for contrastive learning of visual representations," in *Proc. 37th Int. Conf. Mach. Learn.*, 2020, pp. 1597–1607.
- [70] K. Sohn et al., "FixMatch: Simplifying semi-supervised learning with consistency and confidence," in *Proc. Int. Conf. Neural Inf. Process. Syst.*, 2020, vol. 33, pp. 596–608.
- [71] Y. Bengio, A. C. Courville, and P. Vincent, "Representation learning: A review and new perspectives," *IEEE Trans. Pattern Anal. Mach. Intell.*, vol. 35, no. 8, pp. 1798–1828, Aug. 2013.
- [72] D. Ienco, R. Gaetano, R. Interdonato, K. Ose, and D. H. T. Minh, "Combining Sentinel-1 and Sentinel-2 time series via RNN for object-based land cover classification," in *Proc. IEEE Int. Geosci. Remote Sens. Symp.*, 2019, pp. 4881–4884.
- [73] X. Shi, Z. Chen, H. Wang, D. Yeung, W. Wong, and W. Woo, "Convolutional LSTM network: A machine learning approach for precipitation nowcasting," in *Proc. Int. Conf. Neural Inf. Process. Syst.*, 2015, pp. 802–810.
- [74] R. Marc and K. Marco, "Multi-temporal land cover classification with sequential recurrent encoders," *ISPRS Int. J. Geo-Inf.*, vol. 7, no. 4, 2018, Art. no. 129.
- [75] M. Volpi and D. Tuia, "Dense semantic labeling of subdecimeter resolution images with convolutional neural networks," *IEEE Trans. Geosci. Remote Sens.*, vol. 55, no. 2, pp. 881–893, Feb. 2017.
- [76] H. Zhong, C. Chen, Z. Jin, and X. Hua, "Deep robust clustering by contrastive learning," 2020, *arXiv:2008.03030*. [Online]. Available: <https://api.semanticscholar.org/CorpusID:210920406>
- [77] M. Huang and S. Jin, "Rapid flood mapping and evaluation with a supervised classifier and change detection in Shouguang using Sentinel-1 SAR and Sentinel-2 optical data," *Remote Sens.*, vol. 12, no. 13, 2020, Art. no. 2073.
- [78] H. Jung, Y. Oh, S. Jeong, C. Lee, and T. Jeon, "Contrastive self-supervised learning with smoothed representation for remote sensing," *IEEE Geosci. Remote Sens. Lett.*, vol. 19, 2022, Art. no. 8010105.
- [79] E. M. Cuevas, J., and R. Norton, "Inundaciones de 2020 en tabasco: Aprender del pasado para preparar el futuro," Centro Nacional de Prevención de Desastres, Ciudad de México, Mexico, Tech. Rep., 2022. [Online]. Available: https://preparecenter.org/wp-content/uploads/2022/08/PERC_Mexico_ESP.pdf
- [80] M. Tzouvaras, C. Danezis, and D. G. Hadjimitsis, "Differential SAR interferometry using Sentinel-1 imagery-limitations in monitoring fast moving landslides: The case study of Cyprus," *Geosciences*, vol. 10, no. 6, 2020, Art. no. 236.
- [81] D. P. Kingma and J. Ba, "Adam: A method for stochastic optimization," in *Proc. 3rd Int. Conf. Learn. Represent.*, Dec. 2014.
- [82] P. Hurtik, S. Tomasiello, J. Hula, and D. Hynar, "Binary cross-entropy with dynamical clipping," *Neural Comput. Appl.*, vol. 34, pp. 12029–12041, 2022.
- [83] G. Keren, "Neural network supervision: Notes on loss functions, labels and confidence estimation," Ph.D. dissertation, Dept. Faculty Comput. Sci. Math., Univ. Passau, Passau, Germany, 2020.
- [84] M. Vakili, M. K. Ghamsari, and M. Rezaei, "Performance analysis and comparison of machine and deep learning algorithms for IoT data classification," 2020, *arXiv:2001.09636*.



Fernando Pech-May received the master's degree in artificial intelligence from the Center for Research and Advanced Studies, National Polytechnic Institute, Mexico City, Mexico, in 2009, and the Ph.D. degree in computer science from the Centro Nacional de Investigación y Desarrollo Tecnológico, Cuernavaca, Mexico, in 2019.

He is currently a Research Teacher with the Instituto Tecnológico Superior de los Ríos, Tabasco, México. He is currently working on projects related to crop and body monitoring of water using artificial intelligence techniques. He has authored or coauthored different research articles in national and international journals. His research interests include natural language processing, information extraction and retrieval, semantic web, and deep learning.

Dr. Pech-May is a Member of the Topic Group AI for Flood Monitoring and Detection at the International Telecommunication Union.



Raúl Aquino-Santos received the Ph.D. degree in electrical and electronic engineering from the University of Sheffield, Sheffield, U.K., in 2005.

In 2007, he was a Postdoctoral Researcher of Networking and Telecommunications with the Centre for Scientific Research and Higher Education at Ensenada, Ensenada, Mexico. In 2008, he was also a Postdoctoral Researcher of Networking and Telecommunications with the Department of Telecommunications, National Autonomous University of Mexico, Mexico City, Mexico. He is a Member of the National System of Researchers and has authored or coauthored six books, 12 chapters of books, and more than 30 published articles in international journals. His research interests include the design, development, and implementation of Industry 4.0, Internet of Things, Smart Cities, and Natural Disaster Management. He has participated in the International Visitor Leadership Program "Advanced Informatics and Communications Technologies" in the USA, a project for Mexico from the U.S. Department of State Bureau of Educational and Cultural Affairs (2010) and represented Mexico (2014 and 2015) at Asian Pacific Economic Cooperation held in Shanghai, China.

Dr. Aquino-Santos is the Chair of the Topic Group AI for Flood Monitoring and Detection at the International Telecommunication Union.



Omar Álvarez-Cárdenas received the master's degree in telematics and the Ph.D. degree in education from the University of California, Los Angeles, CA, USA, both specialized in active learning using remote laboratories applied to satellite communications, in 1999 and 2018.

He is currently a Research Professor of Mobile Computing Area with the School of Telematics, University of Colima, Colima, Mexico. His research interests include wireless networks, satellite communications, remote laboratories, cybersecurity, and active

learning methodologies.



Jorge Lozoya Arandia received the master's degree in information technologies and the doctorate degree in energy and water from the University of Guadalajara, Guadalajara, Mexico, in 2013 and 2021.

He is an Engineer in communications and electronics. He develops data analysis and computer systems projects, with a specialty in energy optimization, dissemination of image science, and analysis through deep learning. He actually works in natural sensors to develop natural analysis of ecosystems. His research interests include high-performance computing, energy, and digital literacy.

Mr. Arandia is a Member of the National System of Researchers.



German Rios-Toledo received the Ph.D. degree in computer science from the Centro Nacional de Investigación y Desarrollo Tecnológico, Cuernavaca, México, in 2019.

He is currently a Full-Time Professor with the Computer Department, National Technology of Mexico, Tuxtla Gutierrez, Mexico. His main research interests include natural language processing, particularly the use of syntactic information as a feature of writing style. His main research interests also include traditional machine learning algorithm and deep learning applied to the processing of images, audio, and video.